Supporting information for

MXene/Nanocellulose/carbon sphere composite films with multistage "egg-box" structure for electromagnetic interference shielding and pressure sensor

Lansheng Wei [a, b, 1], Yu Ren [a, 1], Yujie Hou [a], Peng Jin [a], Yonghua Zheng [a], Zhengguo Wu [a, *]

[a] College of Food Science and Technology, Nanjing Agricultural University, Nanjing, 210095, China

[b] School of Chemistry and Chemical Engineering, Guangxi Minzu University, Nanning, 530006, China

[1]These authors contribute equally to this work.

[*]Corresponding author:

E-mail address: wuzg@njau.edu.cn (Asso. Prof. ZG. Wu)

The supporting information included 18 Figures and 5 Tables.

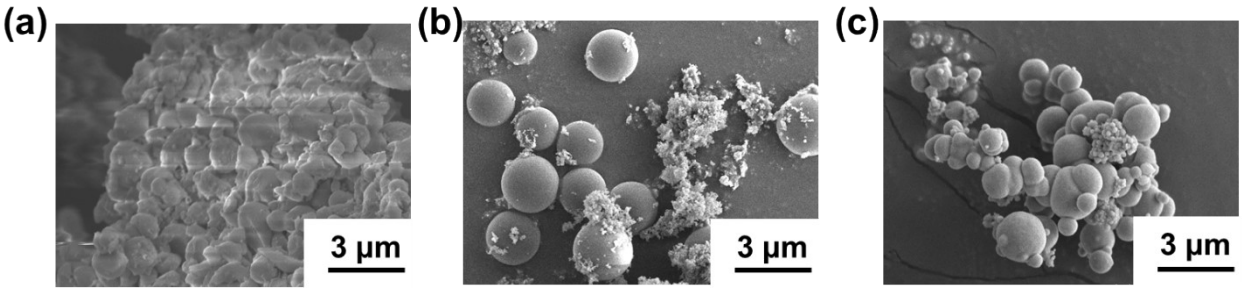

Fig. S1. SEM images of CNCS obtained through hydrothermal reaction at different H_2SO_4 concentrations: (a) 0.5 M, (b) 1 M, and (c) 2 M. Under the catalytic influence of sulfuric acid, cellulose nanocrystals (CNC) undergo hydrolysis during the hydrothermal reaction, leading to the fragmentation of their molecular chains into smaller molecular-weight sugar units. These units subsequently undergo dehydration and condensation, reaggregating to form nuclei that eventually develop into spherical carbon materials. As depicted in **Fig. S1**, the concentration of sulfuric acid significantly affects the morphology of the resulting CNC carbon spheres. Carbon derived from a 1 M sulfuric acid solvent system (**Fig. S1b**) exhibits superior morphological homogeneity compared to that obtained from 0.5 M (**Fig. S1a**) and 2 M (**Fig. S1c**) sulfuric acid solutions. This phenomenon can be attributed to the fact that, within a certain concentration range, an increase in H^+ concentration accelerates the hydrolysis of CNC, resulting in a higher yield of small-molecule structures. These low-molecular-weight substances are more prone to palletization during the hydrothermal process than their high-molecular-weight polymer counterparts [1,2]. Conversely, when the pH of the reaction system is significantly lowered, the spherical carbon nuclei undergo further fusion under the influence of excess acid, culminating in an uneven particle size distribution among the carbon spheres[3].

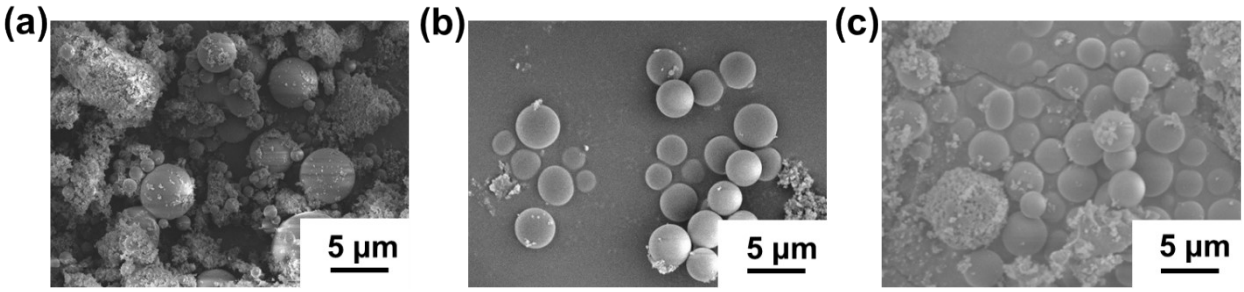

Fig. S2. SEM images of CNCS obtained by hydrothermal reaction time (a) 12 h, (b) 24 h and (c) 36 h. Under acidic conditions, the hydrolytic cleavage and dehydration nucleation of CNC require sufficient reaction times. Insufficient reaction durations lead to incomplete transformation of hydrolysis-derived small molecule products, which subsequently adhere to the surfaces of incipient carbon nuclei, yielding a rough and irregular morphology (**Fig.S2a**). At a reaction time of approximately 24 hours, the nucleation and coalescence of carbon spheres are nearly complete, producing optimally spherical shapes and uniform dispersion (**Fig.S2b**). However, extending the reaction time further initiates fusion among partially formed carbon spheres under acidic conditions, resulting in increased diameters and reduced dispersion (**Fig.S2c**).

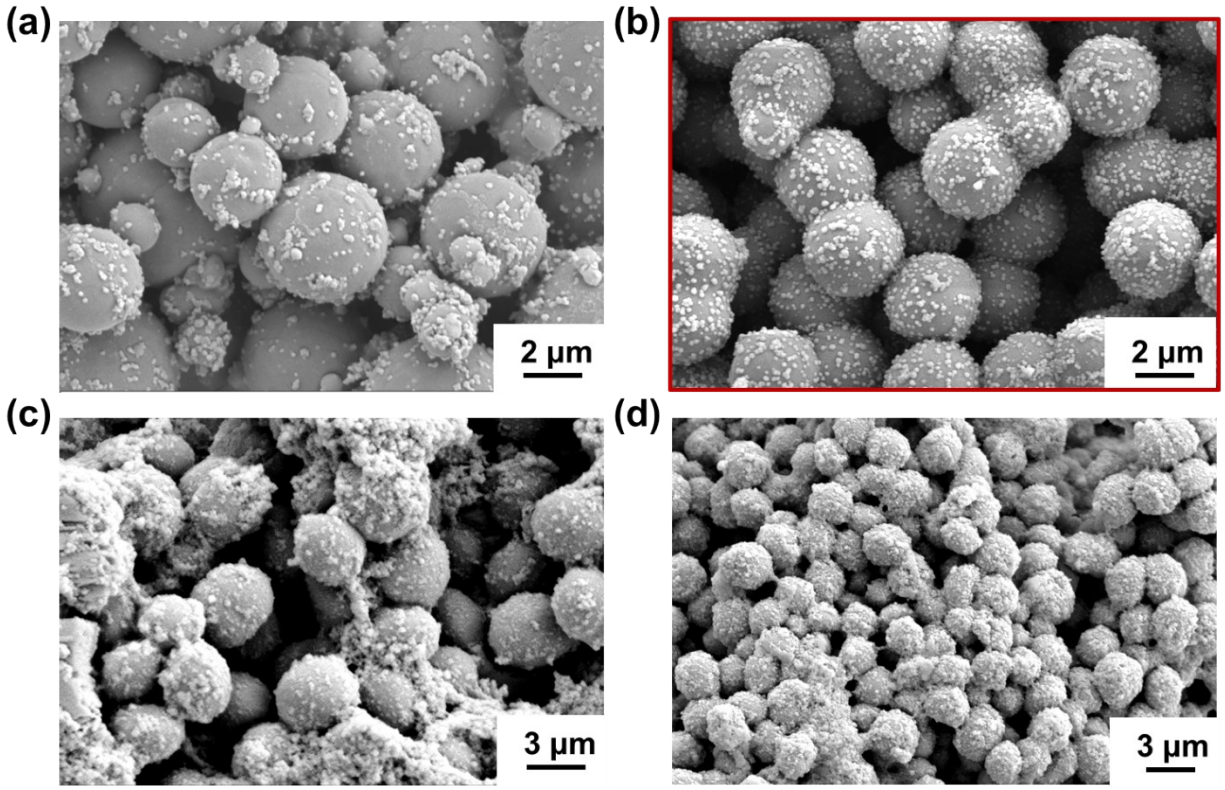

Fig. S3. SEM images of AgNPs@CNCS with different Ag content: (a) 0.1 M, (b) 0.2 M, (c) 0.5 M and (c) 1 M. Insufficient silver content results in inadequate coverage of the carbon spheres' surfaces with silver nanoparticles (**Fig. S3a**). The optimal structural morphology, characterized by a hemp doughnut-like structure, is achieved at a silver concentration of 0.2 M (**Fig. S3b**). However, increasing the silver concentration further leads to aggregation of silver nanoparticles on the carbon spheres' surfaces (**Fig. S3c-d**), which may adversely affect electrical conductivity and limit practical applications.

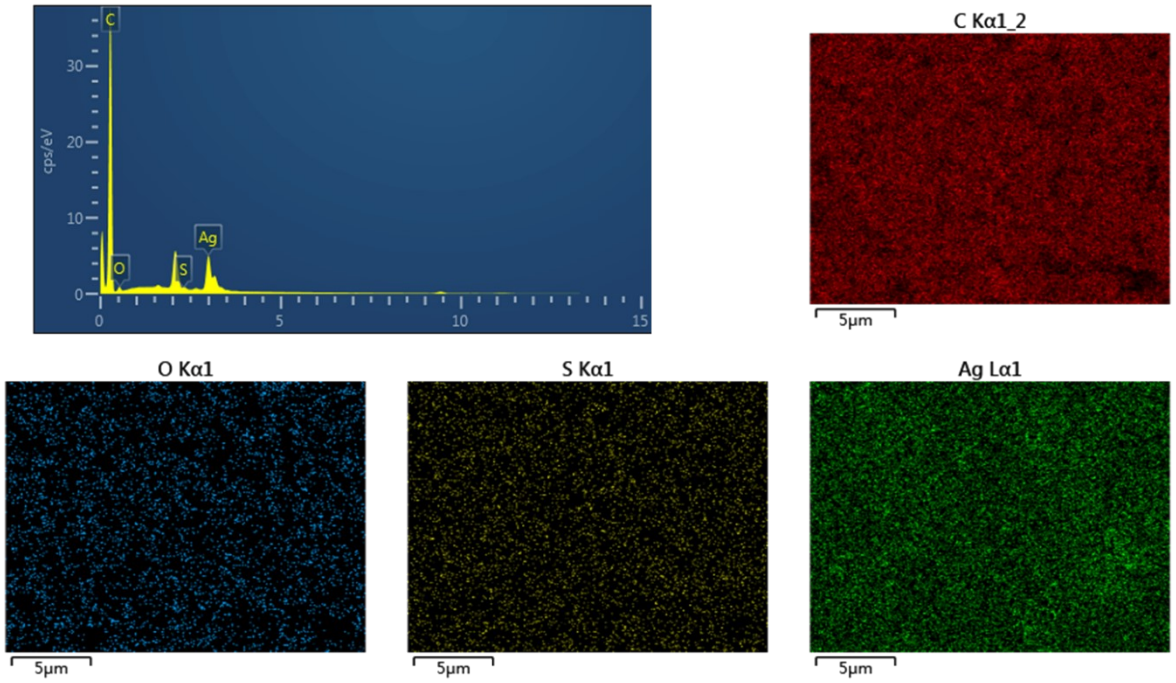

Fig. S4 Elemental content and corresponding distribution of AgNPs@CNCS-2.

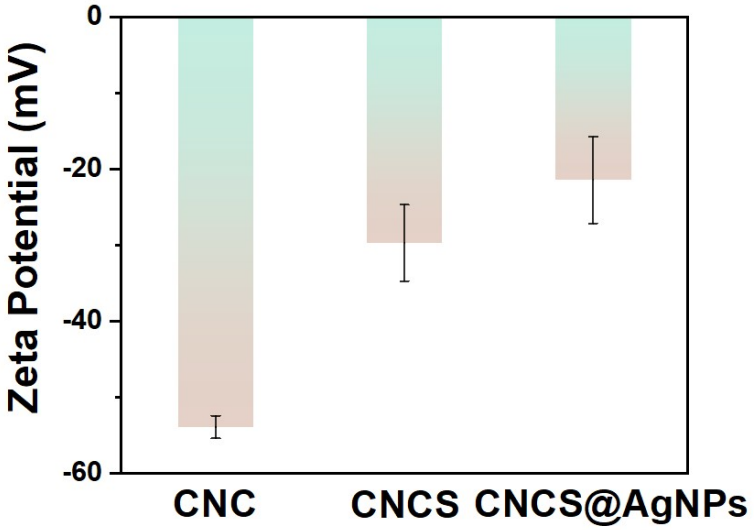

Fig. S5. Zeta potential value CNC, CNCS and AgNPs@CNCS.

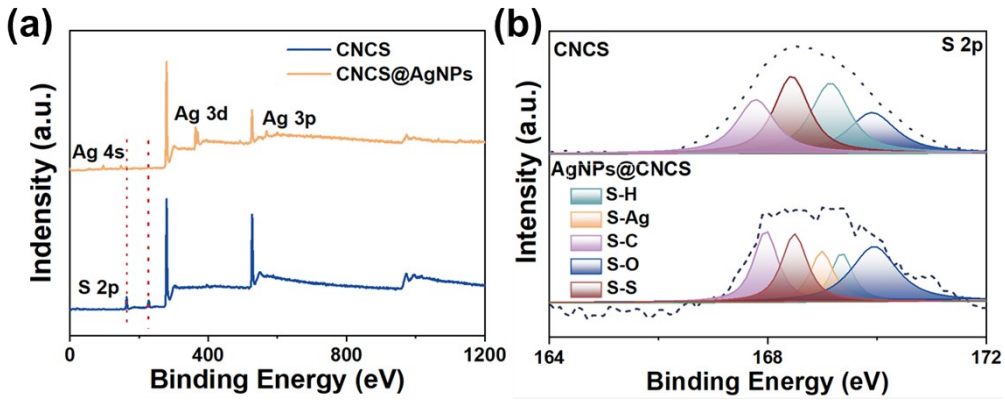

Fig. S6. (a) Full XPS spectra of CNCS and AgNPs@CNCS and (b) the C 1s high-resolution spectra of CNCS and AgNPs@CNCS.

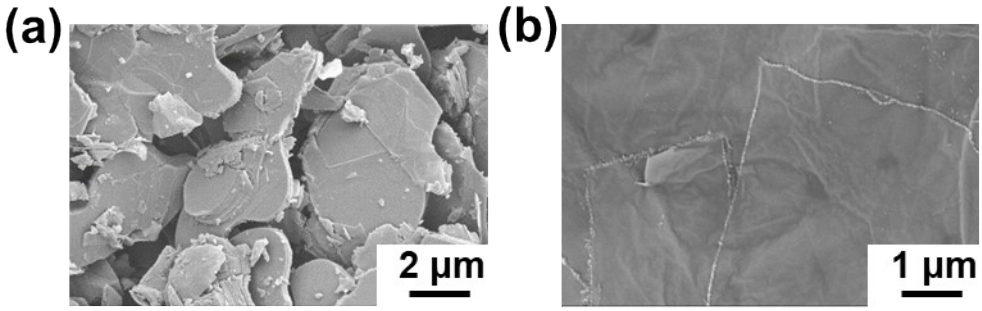

Fig. S7. SEM images of (a) MAX phase and (b) MXene nanosheets.

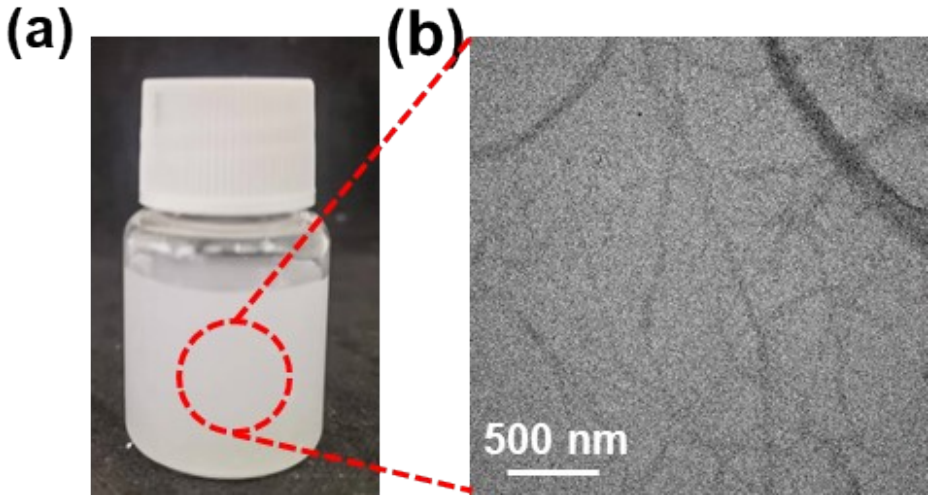

Fig. S8. (a) Optical photograph and (b) TEM images of CNF.

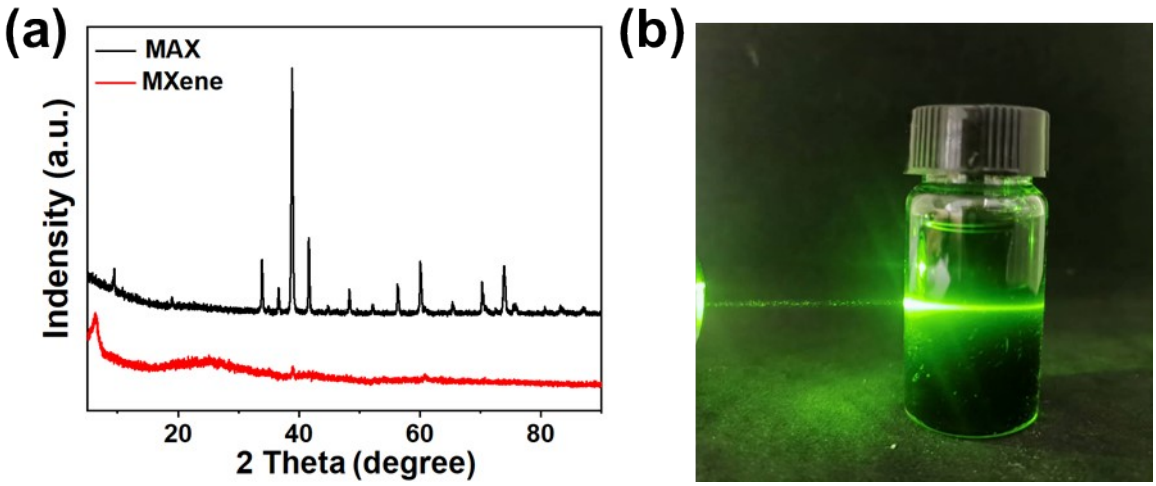

Fig. S9. (a) XRD of MAX phase and MXene; (b) The Tyndall effect in MXene solution.

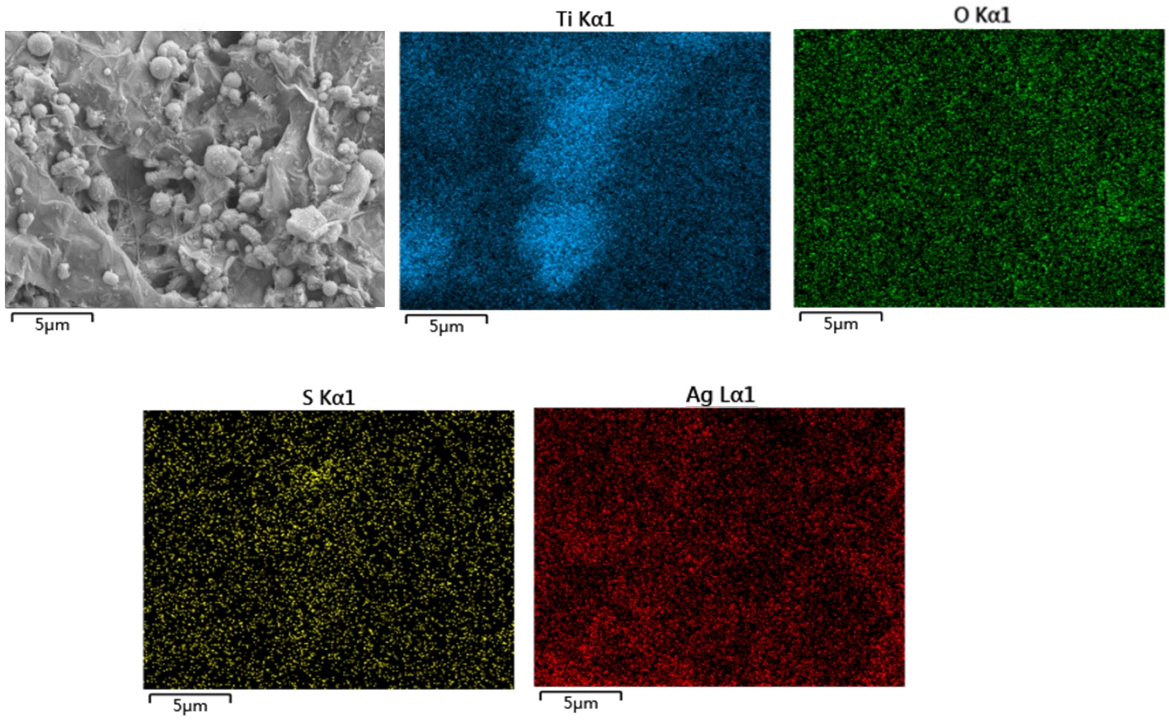

Fig. S10. SEM top-section images and corresponding element (Ti, O, S, Ag) mapping of AgNPs@CNCS/MXene/CNF (ACMN) composite films.

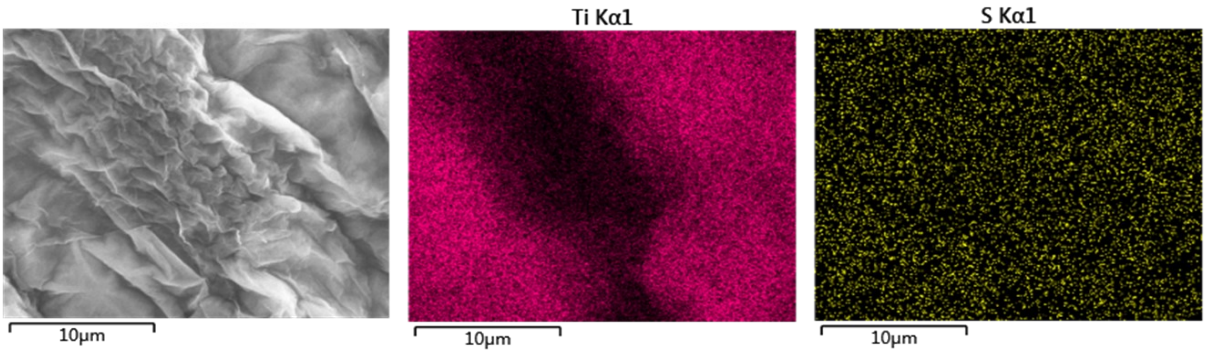

Fig. S11. SEM top-section images and corresponding element (Ti, O, S) mapping of CNCS/MXene/CNF (CMN) composite films.

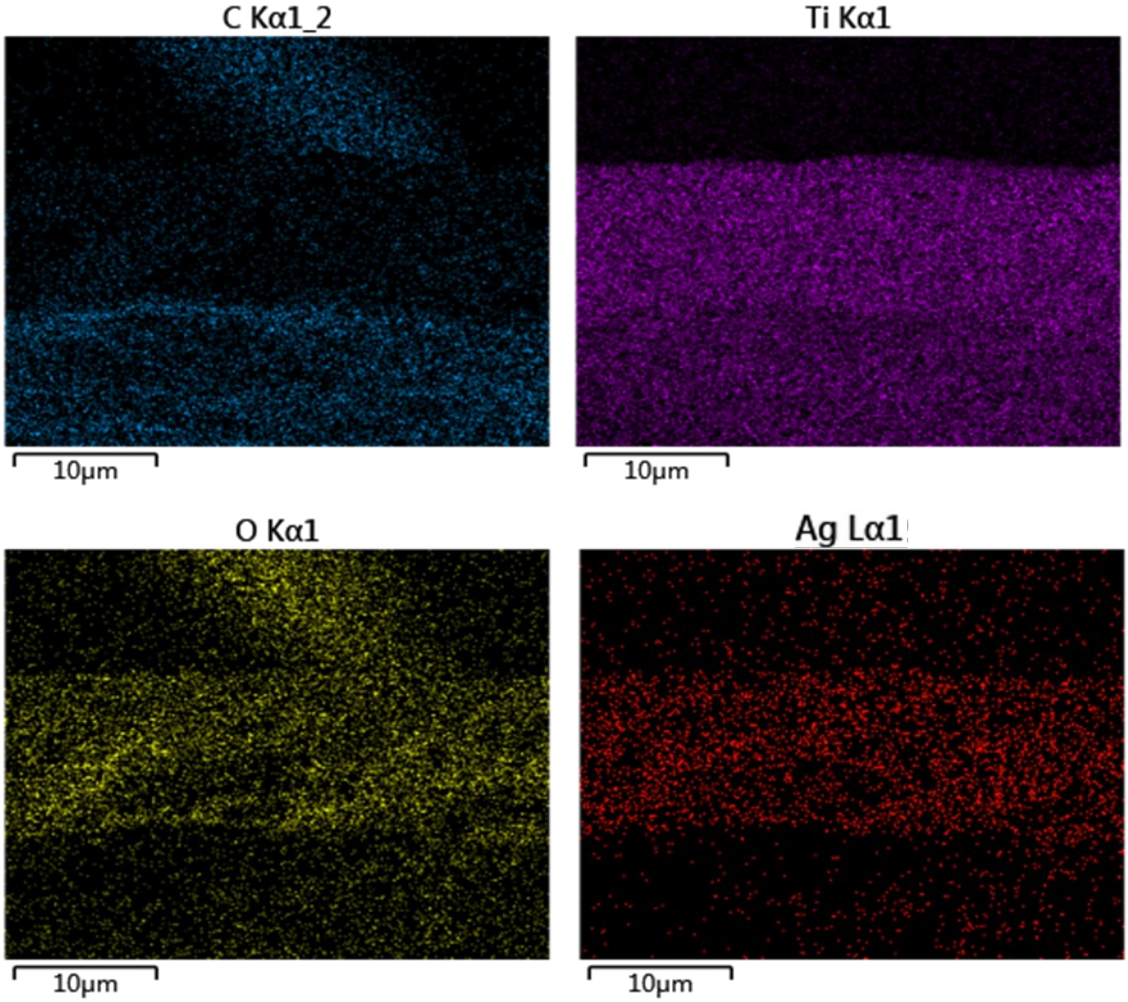

Fig. S12. Element (Ti, O, C, Ag) mappings of the side-section of AgNPs@CNCS/MXene/CNF (ACMF) composite films.

Fig. S13. Optical image of AgNPs@CNCS/MXene film.

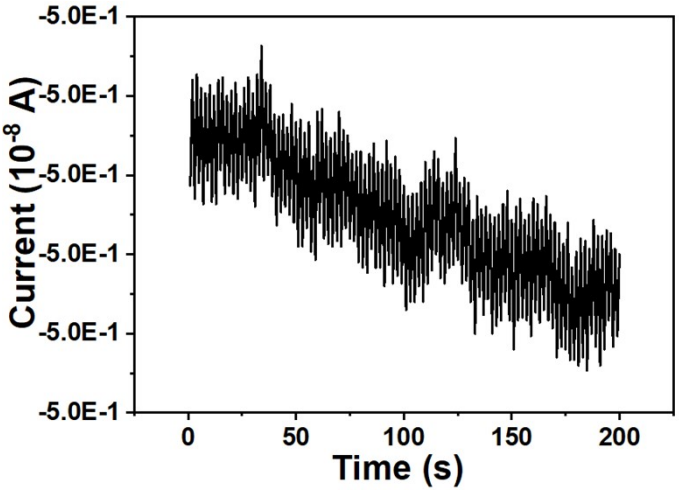

Fig. S14. (a) Natural fluctuation of the ACMF sensor under no pressure.

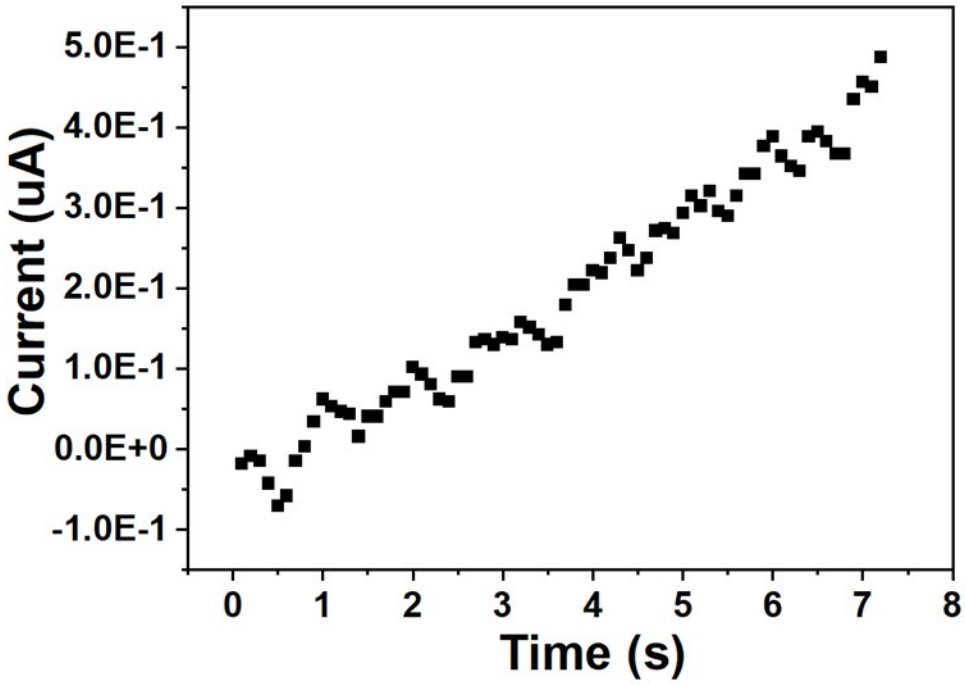

Fig. S15. The real-time current changing curve of the sensor with pressure increasing.

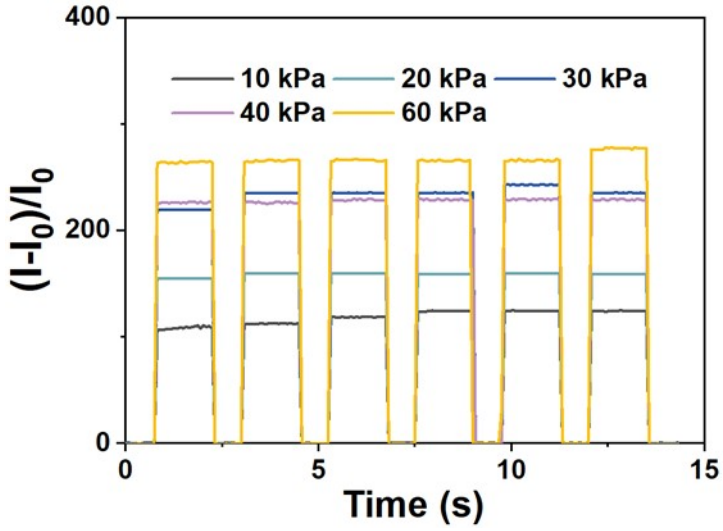

Fig. S16. Current response of CMF sensor.

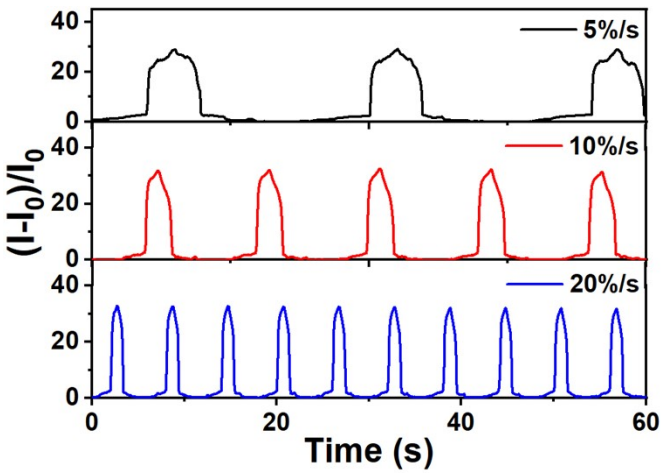

Fig. S17. Different speed response of ACMF sensor under 10 kPa.

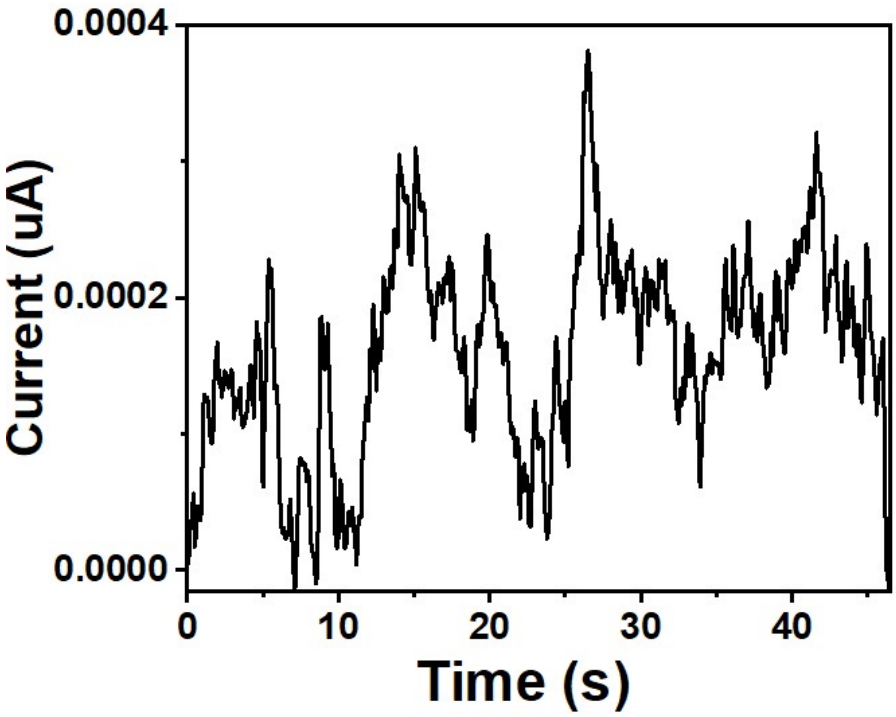

Fig. S18. Pulse test for current response.

Table S1 Elemental analysis of CNC, CNCS and AgNPs@CNCS.

Sample	**CNC**	**CNCS**	**AgNPs@CNCS**
Atomic compositions (%)			
O	37.25	22.06	21.75
C	62.75	75.71	69.68
S	-	2.24	1.64
Ag	-	-	5.93

Table S2 Surface chemical properties of CNCS and AgNPs@CNCS.

Sample	CNCS	AgNPs@CNCS
C 1s compositions (%)		
C─C	26.00	29.74
C─OH	26.46	17.44
C─O─C	23.52	15.51
C═O	24.02	25.26
C─Ag	-	12.05
O 1s compositions (%)		
C─OH	16.82	17.32
C─O─C	19.27	20.67
C─O─O	29.56	27.01
C═O	34.35	35.00
S 2p compositions (%)		
C-S		
S-H	-	11.94
S-O	-	31.43
S-Ag	-	56.63

Table S3 Elemental analysis of AgNPs@CNCS with different AgNPs: CNCS ratios.

Sample	C (wt%)	O (wt%)	S (wt%)	Ag (wt%)
AgNPs@CNCS1	71.21	23.02	3.91	1.86
AgNPs@CNCS2	69.16	24.59	3.71	2.54
AgNPs@CNCS3	70.02	21.95	3.29	4.74

Table S4 Comparison of ACMF composite films with reported EMI shielding materials.

Materials	Thickness (μm)	SE_T (dB)	R	Ref.
NFC/Fe_3O_4-5&CNT/PEO-4	/	29.7	0.9	[4]
FA&MXene/CNF	120	63.8	0.67	[5]
MXene/FeCo/CNF	340	58.0	0.61	[6]
MXene/ANF	225	40.6	0.97	[7]
Graphene/CNF	40	34.9	0.9	[8]
MXene/CNF	35	39.6	0.967	[9]
TRGO@Ni/CNF	/	32.2	0.94	[10]
MXene/PVDF	17	42.9	0.9	[11]
CNT&RGF/PC	200	43.5	0.63	[12]
CNT/PP	200	32.0	0.75	[13]
CF@TiO_2/C	234	74.38	0.8	[14]
CNT/MXene/CoNi	450	49.3	0.78	[15]
ACMF	**54.73**	**74.53**	**0.42**	**This work**

Table S5 Detailed comparison of performance parameters between the fabricated sensor and other recently reported multilayered or microstructure-based pressure sensors.

Sensor	Sensitivity (kPa^{-1})	Detection limit (Pa)	Detection range (kPa)	Response time/ Recovery time (ms)	Cycle number	Ref
CF@TiO_2/C	7.41	/	40	/	100	[14]
rGO/PVDF	47.7	1.3	0-353	40/20	5 000	[16]
CNT/Ni-fabrics	26.13	200	0.2–982	83/88	1 000	[17]
MXene/rGO	22.56	100	1-3.5	245/212	10000	[18]
MXene/NMC	24.63	20	2-20	14/16	5000	[19]
MXene/Silk fibroin	25.56	20	0.1-50	40/35	10000	[20]
MXene/ANF	16.73	80	0.08-100	100/160	5000	[21]
ACMF	**106**	**15**	**0-120**	**50/60**	**10 000**	**This work**

References

1. Sun, X. M.; Li, Y. D., Colloidal carbon spheres and their core/shell structures with noble-metal nanoparticles. Angewandte Chemie-International Edition 2004, 43 (5), 597-601.

2. Falco, C.; Baccile, N.; Titirici, M.-M., Morphological and structural differences between glucose, cellulose and lignocellulosic biomass derived hydrothermal carbons. Green Chemistry 2011, 13 (11), 3273-3281.

3. Karayildirim, T.; Sinag, A.; Kruse, A., Char and Coke Formation as Unwanted Side Reaction of the Hydrothermal Biomass Gasification. Chemical Engineering & Technology 2008, 31 (11), 1561-1568.

4. Li, Y.; Xue, B.; Yang, S.; Cheng, Z.; Xie, L.; Zheng, Q., Flexible multilayered films consisting of alternating nanofibrillated cellulose/Fe3O4 and carbon nanotube/polyethylene oxide layers for electromagnetic interference shielding. Chemical Engineering Journal 2021, 410.

5. Guo, Z.; Ren, P.; Wang, J.; Tang, J.; Zhang, F.; Zong, Z.; Chen, Z.; Jin, Y.; Ren, F., Multifunctional sandwich-structured magnetic-electric composite films with Joule heating capacities toward absorption-dominant electromagnetic interference shielding. Composites Part B-Engineering 2022, 236.

6. Ma, M.; Tao, W.; Liao, X.; Chen, S.; Shi, Y.; He, H.; Wang, X., Cellulose nanofiber/MXene/FeCo composites with gradient structure for highly absorbed electromagnetic interference shielding. Chemical Engineering Journal 2023, 452.

7. Weng, C.; Xing, T.; Jin, H.; Wang, G.; Dai, Z.; Pei, Y.; Liu, L.; Zhang, Z., Mechanically robust ANF/MXene composite films with tunable electromagnetic interference shielding performance. Composites Part a-Applied Science and Manufacturing 2020, 135.

8. Li, L.; Ma, Z.; Xu, P.; Zhou, B.; Li, Q.; Ma, J.; He, C.; Feng, Y.; Liu, C., Flexible and alternant-layered cellulose nanofiber/graphene film with superior thermal conductivity and efficient electromagnetic interference shielding. Composites Part a-Applied Science and Manufacturing 2020, 139.

9. Zhou, B.; Zhang, Z.; Li, Y.; Han, G.; Feng, Y.; Wang, B.; Zhang, D.; Ma, J.; Liu, C., Flexible,

Robust, and Multifunctional Electromagnetic Interference Shielding Film with Alternating Cellulose Nanofiber and MXene Layers. Acs Applied Materials & Interfaces 2020, 12 (4), 4895-4905.

10. Han, G.; Ma, Z.; Zhou, B.; He, C.; Wang, B.; Feng, Y.; Ma, J.; Sun, L.; Liu, C., Cellulose-based Ni-decorated graphene magnetic film for electromagnetic interference shielding. Journal of Colloid and Interface Science 2021, 583, 571-578.

11. Li, Y.; Zhou, B.; Shen, Y.; He, C.; Wang, B.; Liu, C.; Feng, Y.; Shen, C., Scalable manufacturing of flexible, durable $Ti_3C_2T_x$ MXene/Polyvinylidene fluoride film for multifunctional electromagnetic interference shielding and electro/photo-thermal conversion applications. Composites Part B-Engineering 2021, 217.

12. Yu, W.-C.; Wang, T.; Liu, Y.-H.; Wang, Z.-G.; Xu, L.; Tang, J.-H.; Dai, K.; Duan, H.-J.; Xu, J.-Z.; Li, Z.-M., Superior and highly absorbed electromagnetic interference shielding performance achieved by designing the reflection-absorption-integrated shielding compartment with conductive wall and lossy core. Chemical Engineering Journal 2020, 393.

13. Zhang, Y.-P.; Zhou, C.-G.; Sun, W.-J.; Wang, T.; Jia, L.-C.; Yan, D.-X.; Li, Z.-M., Injection molding of segregated carbon nanotube/polypropylene composite with enhanced electromagnetic interference shielding and mechanical performance. Composites Science and Technology 2020, 197.

14. Wu, F.; Hu, F.; Hu, P.; Zhang, P.; Fan, B.; Kong, H.; Zheng, W.; Cai, L.; Sun, Z., Multifunctional carbon Fiber@TiO_2/C aerogels derived from MXene for pressure tunable microwave absorption. Carbon 2024, 230.

15. Gao, Y.; Chen, X.; Jin, X.; Zhang, C.; Zhang, X.; Liu, X.; Li, Y.; Li, Y.; Lin, J.; Gao, H.; Wang, G., Multifunction integration within magnetic CNT-bridged MXene/CoNi based phase change materials. Escience 2024, 4 (6).

16. Zhu, Y.; Hartel, M. C.; Yu, N.; Garrido, P. R.; Kim, S.; Lee, J.; Bandaru, P.; Guan, S.; Lin, H.; Emaminejad, S.; de Barros, N. R.; Ahadian, S.; Kim, H.-J.; Sun, W.; Jucaud, V.; Dokmeci, M. R.; Weiss, P. S.; Yan, R.; Khademhosseini, A., Epidermis-Inspired Wearable Piezoresistive

Pressure Sensors Using Reduced Graphene Oxide Self-Wrapped Copper Nanowire Networks. Small Methods 2022, 6 (1).

17. Zhao, Y.; Li, X.; Hou, N.; Huang, S.; Yuan, T.; Wang, H.; Zhang, A.; Li, X.; Zhang, W., Ultra-thin self-powered sensor integration system with multiple charging modes in smart home applications. Materials Today Nano 2023, 23.

18. Ma, Y.; Yue, Y.; Zhang, H.; Cheng, F.; Zhao, W.; Rao, J.; Luo, S.; Wang, J.; Jiang, X.; Liu, Z.; Liu, N.; Gao, Y., 3D Synergistical MXene/Reduced Graphene Oxide Aerogel for a Piezoresistive Sensor. Acs Nano 2018, 12 (4), 3209-3216.

19. Wang, K.; Lou, Z.; Wang, L.; Zhao, L.; Zhao, S.; Wang, D.; Han, W.; Jiang, K.; Shen, G., Bioinspired Interlocked Structure-Induced High Deformability for Two-Dimensional Titanium Carbide (MXene)/Natural Microcapsule-Based Flexible Pressure Sensors. ACS Nano 2019, 13 (8), 9139-9147.

20. Wang, D.; Wang, L.; Lou, Z.; Zheng, Y.; Wang, K.; Zhao, L.; Han, W.; Jiang, K.; Shen, G., Biomimetic, biocompatible and robust silk Fibroin-MXene film with stable 3D cross-link structure for flexible pressure sensors. Nano Energy 2020, 78.

21. Su, T.; Liu, N.; Lei, D.; Wang, L.; Ren, Z.; Zhang, Q.; Su, J.; Zhang, Z.; Gao, Y., Flexible MXene/Bacterial Cellulose Film Sound Detector Based on Piezoresistive Sensing Mechanism. ACS Nano 2022, 16 (5), 8461-8471.